Cell

Active Remodeling of Cortical Actin Regulates Spatiotemporal Organization of Cell Surface Molecules

Kripa Gowrishankar,[1,3] Subhasri Ghosh,[1,3] Suvrajit Saha,[2] Rumamol C.,[2] Satyajit Mayor,[2,*] and Madan Rao[1,2,*]
[1]Raman Research Institute, C.V. Raman Avenue, Sadashivanagar, Bangalore 560080, India
[2]National Centre for Biological Sciences (TIFR), Bellary Road, Bangalore 560065, India
[3]These authors contributed equally to this work
*Correspondence: mayor@ncbs.res.in (S.M.), madan@ncbs.res.in (M.R.)
DOI 10.1016/j.cell.2012.05.008

SUMMARY

Many lipid-tethered proteins and glycolipids exist as monomers and nanoclusters on the surface of living cells. The spatial distribution and dynamics of formation and breakup of nanoclusters does not reflect thermal and chemical equilibrium and is controlled by active remodeling of the underlying cortical actin. We propose a model for nanoclustering based on active hydrodynamics, wherein cell surface molecules bound to dynamic actin are actively driven to form transient clusters. This consistently explains all of our experimental observations. Using FCS and TIRF microscopy, we provide evidence for the existence of short, dynamic, polymerizing actin filaments at the cortex, a key assumption of the theoretical framework. Our theory predicts that lipid-anchored proteins that interact with dynamic actin must exhibit anomalous concentration fluctuations, and a cell membrane protein capable of binding directly to actin can form nanoclusters. These we confirm experimentally, providing an active mechanism for molecular organization and its spatiotemporal regulation on the plasma membrane.

INTRODUCTION

The living cell surface spatiotemporally regulates its local composition and shape to engage with the outside world. ''Membrane rafts,'' conceived as lipid-based compositional heterogeneities, have been invoked to facilitate these interactions (Lingwood and Simons, 2010; Simons and Ikonen, 1997). Rafts have been postulated to have a thermodynamic origin, wherein compositional heterogeneities result from being at or near phase coexistence (Edidin, 2003). GPI-anchored proteins (GPI-APs) are outer leaflet lipid-anchored protein components of classical lipid rafts; thus, their organization should be consistent with thermodynamic principles. However, properties of the nanoscale spatial organization and dynamics of these cell surface molecules determined using high-resolution techniques such as fluorescence resonance energy transfer (FRET) (Goswami et al., 2008; Sharma et al., 2004; Varma and Mayor, 1998) are not easily accounted for within the existing paradigms for the organization of the plasma membrane (PM).

These studies have shown that GPI-APs are organized as immobile nanoscale clusters and monomers whose fraction is independent of its concentration. This nanoclustering is important as sorting signals for their endocytosis (Sharma et al., 2004). Recent near field scanning optical microscopy provides evidence that confirms such GPI-AP clustering (van Zanten et al., 2009). In addition, it shows that this GPI-AP organization reports on the generation of an appropriate lipid environment that is necessary for integrin signaling. The spatial distribution of nanoclusters is sensitive to perturbations of membrane cholesterol levels, the cortical actin (CA) cytoskeleton, and its actomyosin contractility (Goswami et al., 2008). The GPI-AP clustering is dynamic, with fast aggregation-fragmentation rates, dependent on actomyosin activity. Furthermore, nanoclusters fragment into monomers where the cell membrane has detached from the CA, as in spontaneously formed blebs, and are reformed when blebs retract due to the repolymerization of actin. Studies of the steady-state distributions of two other classes of lipid-tethered molecules, Ras-signaling proteins (Plowman et al., 2005) and glycolipids (Fujita et al., 2007), by electron microscopy (EM) have also indicated nonrandom mixtures of nanoclusters and monomers dependent on CA. This nanoscale clustering is necessary for the switch-like response of Ras signaling (Kholodenko et al., 2010). Taken together, these observations suggest an unusual kind of molecular organization driven by the ATP-fueled (active) dynamics of CA rather than conventional protein-protein interactions or lipid-phase segregation (Mayor and Rao, 2004). Correspondingly, the active distribution and remodeling dynamics of GPI-AP nanoclusters on the cell surface demand an active composite cell surface that intimately couples membrane components with CA activity.

The CA meshwork is usually regarded as being built from long, static, crosslinked cortical actin filaments oriented tangential to the PM punctuated by bundles of vertical actin. This forms a scaffold or mesh that influences the spatial patterning of membrane components. This picture is a result of several experiments, including cell surface microrheology (Sheetz et al., 2006),

cryo-EM (Morone et al., 2006; Svitkina and Borisy, 1999), and single-particle tracking (SPT) (Fujiwara et al., 2002). However, to explain the active actomyosin-based formation, distribution, and remodeling dynamics of GPI-AP nanoclusters on the flat regions of the cell surface, we propose that, in addition to the stable CA meshwork, there is a population of shorter dynamic actin filaments undergoing actomyosin contractility (Figure 1).

Here, we explore the consequences of this two-species model of the CA using theoretical considerations drawn from active hydrodynamics. We test and verify key assumptions of the theoretical proposal, namely the existence of shorter, dynamic, polymerizable actin filaments at the cortex, using FCS and TIRF microscopy. We then make several testable (in principle, falsifiable) predictions, which we confirm using fluorescence-based experiments. Our analyses indicate that lipid-tethered cell surface molecules must bind dynamic cortical actin to be able to form nanoclusters.

RESULTS

Theoretical Rationale for Dynamic Actin Filaments at the Cortex

To explain the actomyosin-dependent dynamics and the nanoscale organization of GPI-anchored proteins, we propose that, amidst the relatively static CA meshwork, dynamic actin filaments adjoining the inner leaflet of the PM in conjunction with a remodeling actomyosin machinery give rise to tangential active stresses and currents on the membrane (Figure S1 available online). The active dynamics of these filaments must consist of the following stochastic processes (Figure 1): (1) binding/unbinding of filaments onto the inner leaflet of the PM via membrane binding proteins; (2) polymerization/depolymerization, which result in treadmilling and a distribution of filament lengths (Howard, 2001); (3) binding of myosin-like motors onto the filaments, which results in ATP-dependent crosslinking of filaments and generation of contractile stresses and currents, leading to local changes in filament position and orientation (Howard, 2001); and (4) interaction with the static actin meshwork. In general, these processes result in active stresses that act both normal and tangential to the plasma membrane—the former predominantly affecting its shape and the latter its composition via particle currents derived from active particle stresses (see additional details in Theory Sections I and II in Extended Experimental Procedures).

To quantitatively understand the consequences of these active stresses, we take a coarse-grained theoretical approach (see Theory Section I in Extended Experimental Procedures). Thus, we describe the active remodeling dynamics of polar actin filaments by their local concentration, $c(\mathbf{r},t)$, polar orientation, $\mathbf{n}(\mathbf{r},t)$, and apolar orientation tensor, $\mathbf{Q}(\mathbf{r},t)$ (Toner and Tu, 1998; Ramaswamy, 2010). To keep the discussion simple, we will focus on polar filaments with polar ordering; in this case, it suffices to describe the dynamics of c and $\mathbf{n}$. In the Discussion, we point out the implications of having an apolar ordering of polar filaments.

Being actively driven out of equilibrium, the polar filament orientation $\mathbf{n}$ implies a local average drift velocity of the active filaments relative to the fluid; it is this interpretation of $\mathbf{n}$ that we will follow henceforth. We ignore the hydrodynamic velocity because it is damped by local friction $\Gamma = \mu/\xi^2$ through the cytoskeletal meshwork, with mesh size ξ and cortical viscosity μ (see explanation in Theory Section I in the Extended Experimental Procedures). The effect of the long, static actin filaments on the dynamics of the shorter dynamic actin filaments depends on the scale L at which we probe the dynamics.

Rapid-freeze EM tomography of the cortical mesh in a number of cell types reveals that the local mesh size ranges from 20–500 nm, with a typical size $\xi \approx 250$ nm (Morone et al., 2006). If $L \ll \xi$, then the static filaments provide boundary anchoring conditions on n and c. On the other hand, if $L \gg \xi$, then the static meshwork provides a random anchoring to the dynamic actin filaments (in other words, it acts as a quenched random anchoring field), which when averaged over a scale larger than ξ (but smaller than L) leads to dynamical equations in $\mathbf{n}$ and c, with parameters reflecting the position and orientation distribution of the static filaments. In either case, the dynamics for $\mathbf{n}$ and c is given by:

$$\partial_t \mathbf{n} = \underbrace{-\lambda(\mathbf{n}\cdot\nabla)\mathbf{n}}_{\text{relative sliding}} + \overbrace{K_1\nabla^2\mathbf{n} + K_2\nabla(\nabla\cdot\mathbf{n})}^{\text{relative alignment}} + \underbrace{\zeta\nabla c}_{\text{contractility}} + \underbrace{\alpha\mathbf{n} - \beta|\mathbf{n}|^2\mathbf{n}}_{\text{spontaneous polarization}} + \underbrace{\mathbf{f_n}}_{\text{activenoise}} \quad (1)$$

$$\partial_t c = -\nabla\cdot\mathbf{J}_c = -\nabla\cdot\left(\underbrace{v_0 c\mathbf{n}}_{\text{active advection}} - \underbrace{D_f\nabla_c}_{\text{diffusion}}\right) \quad (2)$$

The terms on the right of (1) and (2) represent contributions to the active forces/torques and current $\mathbf{J_c}$, whose physical origins are schematically described in Figure 1. The sliding and advection terms above are uniquely active effects. Noise in the active forces, given by $\mathbf{f_n}$, reflects the stochasticity in the interactions of the dynamic actin filaments with the myosin-like motors, whose statistics we discuss later.

The parameters entering Equations 1 and 2 can be obtained from the microscopic processes of actomyosin dynamics and treadmilling and depend on the characteristics of myosin—duty ratio, stepping rate, and induced relative angular velocity—and those of actin filaments—mean concentration, length, aspect ratio, and treadmilling rates (Theory Sections I and VII in Extended Experimental Procedures). The coefficient $\alpha \propto (\bar{c} - c^*)$ measures the deviation of the mean filament concentration $\bar{c}$ from the "Onsager" value c^* (de Gennes and Prost, 1993), beyond which the filaments exhibit a spontaneous polarization, $|\mathbf{n}| \neq 0$. In this orientationally ordered phase, $\alpha > 0$ *or* $\bar{c} > c^*$, we can construct several length scales of which the most important is the *active Peclet* length, $L_p = D_f/v_0$, which measures the ratio of the diffusion to active advection. All of these parameters depend on the local orientation and concentration of the static filaments and a host of locally regulatable molecules and are thus heterogeneous over the cell surface. The typical values of these parameters that we have used to obtain quantitative results and to compare with experiments (Figures 2 and 3) are given in Theory Section VII in the Extended Experimental Procedures.

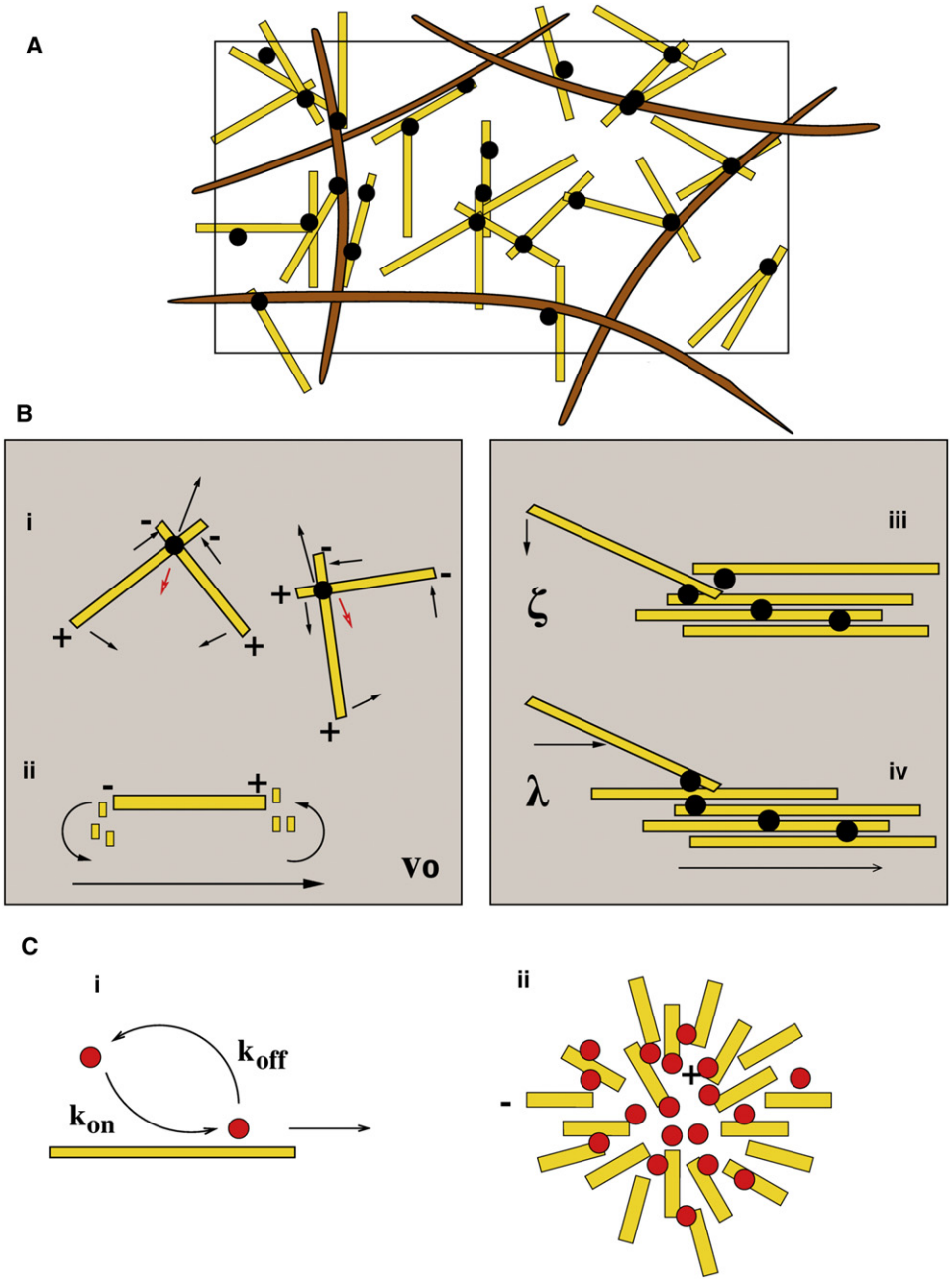

Figure 1. Schematic of Active Composite Membrane: Structure, Forces, and Currents

(A) Patch of PM showing the inner leaflet attached to tangentially disposed CA, consisting of long, crosslinked filaments forming a static, heterogeneous meshwork (brown) and shorter, dynamic filaments (gold), which stochastically (un)bind to the PM and are temporarily crosslinked by myosin motors (black).

(B) (i) Active forces and torques arising from the "walking" of myosin from the minus (−) to plus (+) ends of the filaments (red arrow indicates resultant direction of myosin motion) lead to a spontaneous velocity of the filaments (dark arrow) and an angular velocity (small arrows) that aligns filaments relative to each other. (ii) Differential rates of (de)polymerization at the +/− ends of a filament (treadmilling) lead to a spontaneous velocity (along the black arrow). In a description, coarse grained over a collection of filaments, (i) and (ii) result in a net coarse-grained velocity v_0 along the net coarse-grained filament orientation. (iii) The increased myosin crosslinking in regions rich in filaments can result in peripheral filaments aligning along the average orientation of the filaments and being pulled toward denser regions; this is described by the ζ term in Equation 1. (iv) Similarly, a peripheral filament can be actively advected along the motion of the filament bundle, described by λ.

(C) (i) Passive molecules (red), such as GPI-APs, (un)bind to filaments. The bound molecule then rides (or more technically, is advected) along with the filament (black arrow). (ii) The spontaneous patterning of active filaments into inward-pointing asters drives passive molecules to the cores of the asters to form nanoclusters.

See also Figure S1.

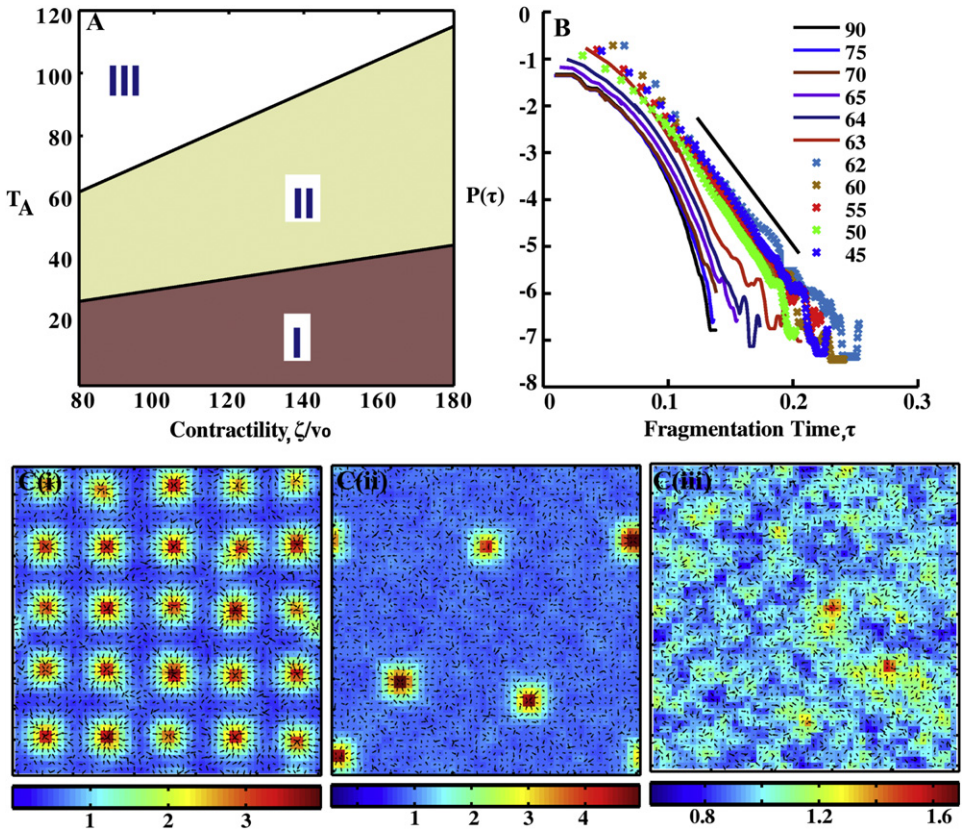

Figure 2. Dynamical Remodeling of Actin Asters Induced by Noise

(A) Phase diagram in the contractility ζ/v_0 versus active temperature T_A plane, obtained by numerically solving Equations 1 and 2, shows three regimes of aster dynamics: (1) small oscillations, (2) power-law remodeling, and (III) exponential remodeling. The dimensionless parameter values chosen are $K_1 = D_f = 5$, $K_2 = 0$, and $\alpha = 100$ (in terms of real values; Extended Experimental Procedures).

(B) Log_e-Log_e plot of the distribution of aster lifetimes $P(\tau)$ for different active temperatures, T_A, shows a crossover from power law (crosses) to exponential (solid curves). Black straight line is a fit to $P(\tau) : \tau^{-2.7}$. The value of the contractility has been chosen to be $\zeta/v_0 = 80$ (see Theory Section VII in Extended Experimental Procedures).

(C) (i)–(iii) are typical snapshots in the three regimes at the same value of contractility, with T_A = 20,54 and 90, respectively. See also Figures S2 and S3.

Dynamic Actin Filaments Form Transient Asters with Characteristic Remodeling Statistics

The two-species model of the CA meshwork leads to specific consequences for the patterning and dynamics of the active actin filaments on the cell membrane. In brief, our results suggest that the active actin filaments organize themselves into stable aster-rich (and -poor) phases as a natural consequence of the presence of adequate concentrations of treadmilling actin and active myosin. The flat cellscapes over which we focus our investigation are large patches on the cell surface that are enriched in cortical actin, and thus the probe scale L is large and the filament concentration is large (i.e., $\alpha>0$ *or* $\bar{c}>c^*$). In this case, *any* amount of contractility, parameterized by ζ, induces an instability in the homogeneous-oriented phase (provided $\zeta v_0>0$), leading to density and orientational patterning arising from a competition between the contractile terms ζ and v_0 and the relaxation terms D_f, K_1, and K_2.

We determine the steady-state configurations by numerically solving Equations 1 and 2, starting from random initial conditions and appropriate boundary conditions (detailed in Theory Section VI in Extended Experimental Procedures). Indeed, a rich phase diagram emerges dependent on filament concentration and myosin contractility (Gowrishankar, 2009; K.G. and M.R., unpublished data). The steady-state configurations generically consist of homogeneous regions where the filaments are oriented roughly parallel to one another, interspersed with a finite density of inward-pointing asters. At high densities, the inward-pointing asters are separated by outward-pointing asters and saddle points that locally expel filaments (Figure 2C). The size of the localized asters is set by L_p, the active Peclet length (Figure S2).

In the presence of active noise, the steady-state configurations exhibit a rapid remodeling of asters (Figure 2). As a consequence, the aster patterns will appear as inhomogeneities in filament concentration and orientation, associated with a nonzero divergence of filament orientation. We explore the consequences of coupling cell membrane components to such a dynamically remodeling actin and show that this provides a natural explanation for all of the unusual properties of the GPI-AP nanoclusters and monomers (Figure S3).

Such actin configurations with filament barbed ends pointing inward and myosin 2 at the cores have been observed in fibroblasts treated with low doses of cytochlasin D (Verkhovsky et al., 1997). They have also been observed in active gels formed by in vitro reconstitutions of actin, myosin 2, and fascin (an actin-bundling protein) with ATP (Backouche et al., 2006; Köhler et al., 2011) and in the presence of actin nucleators such as Arp2/3 and VCA domain of WASP (Haviv et al., 2006).

These aster-like patterns are subject to active spatiotemporal stochasticity $\mathbf{f}_n$ in (1). We take this active noise to be uncorrelated and white, with zero mean and variance proportional to T_A/c, wherein T_A is an active temperature (see explanation in Theory Section I in the Extended Experimental Procedures). As mentioned above, the origins of stochasticity are essentially due to myosin turnover. Spatiotemporal noise leads to a dramatic remodeling of the aster patterns: we find at least three distinct regimes, I–III (Figure 2A), upon increasing the active temperature, T_A. At low T_A (regime I), the asters vibrate about their mean position with an amplitude proportional to T_A (Figure 2Ci). With increasing T_A (regime II), some of the filaments free themselves from their native asters and explore the region between asters (Figure 2Cii), resulting in a decrease in the aster density, $\Phi \equiv \int drc\nabla\cdot n$ (see explanation in Theory Section III in the Extended Experimental Procedures). The interplay between active noise and contractility leads to fragmentation and reformation of asters (Figure 2Ciii) characterized by a remodeling time distribution (Supplemental Information and Figure S2), which shows a sudden change with increasing T_A, going from power-law in regime II to exponential in regime III (Figure 2B). The mean density of asters decreases with increasing active temperature (Supplemental Information and Figure S2), and the rest of the filaments not contained in asters give rise to a net mean orientation $\langle c\ \mathbf{n}\cdot\mathbf{x}\rangle$; this will turn out to be significant later. These transitions are also discussed in greater detail elsewhere (Gowrishankar, 2009; K.G. and M.R., unpublished data).

Dynamics and Clustering of Passive Molecules

The dynamic patterning of the dynamic actin filaments just described is likely to affect the large number of cell surface molecules capable of binding filamentous actin. This influence of actin could be direct, due to the presence of cytoplasmic actin-binding motifs, or indirect either via coupling to actin-binding proteins or via lipid-based transbilayer interactions. We define three classes of cell surface molecules according to their interaction with the underlying dynamic actin filaments: (1) inert, which do not bind to the dynamic actin but couple hydrodynamically with the static mesh; (2) passive, which bind (directly or indirectly) to the dynamic actin but whose dynamics does not affect the actin; and (3) active, whose dynamics, in addition, influences dynamic actin filaments and/or motor activity. Here, we restrict our study to the dynamics of inert and passive molecules.

Consider a collection of passive cell surface molecules described by a local density ρ, which stochastically bind (unbind) onto the dynamic actin filaments with rates $k_{on}(k_{off})$, respectively (Figure 1Ci). Bound passive molecules are advected with a velocity v_0 by the actively moving filaments, whereas unbound molecules freely diffuse on the membrane with a diffusion coefficient D,

$$\partial_t\rho = -\nabla\cdot\mathbf{J}_\rho = -\nabla\cdot(\phi(\mathbf{r},t)\rho\mathbf{v}_0\mathbf{n} - (1-\phi(\mathbf{r},t))D\nabla\rho - \mathbf{f}_\rho) \quad (3)$$

in which the additive noise $\mathbf{f}_\rho$ is thermal in origin with zero mean and variance proportional to k_BTD, and the multiplicative noise φ describes the statistics of (un)binding (Langmuir kinetics, obeying detailed balance), with a mean characterized by the duty ratio $K_d = k_{on}c/(k_{on}c + k_{off})$ and temporal fluctuations by a switching time $t_{sw} = 2/(k_{on}c + k_{off})$, in which C is the local concentration of actin filaments.

The activity-driven formation of inward-pointing actin asters will readily focus bound passive molecules to the aster cores, leading to an active mechanism of cluster formation (Figure 1Cii) that is distinct from the usual thermodynamic mechanism of clustering due to protein-protein interactions. The mean cluster size, obtained from the exponential fall-off of the passive molecule density away from the aster core, is set by the duty ratio K_d, aster size L_p, and the active temperature T_A (see Theory Section III in the Extended Experimental Procedures). With increasing K_d, the cluster size shows a sigmoidal increase, saturating roughly at the size of the underlying aster (Supplemental Information and Figure S2D). With increasing active temperature T_A, the mean cluster size decreases slowly at first (regime I) and then rapidly to a small value in regimes II and III (Supplemental Information and Figure S2E). The remodeling dynamics of the actin asters in regimes II and III (Supplemental Information and Figure S2C) leads to the fragmentation and reformation of the passive molecule nanoclusters; consequently, the density of passive molecules exhibits large spatiotemporal fluctuations (Figure S3Aii).

The active temperature dependence of the mean cluster size suggests that those passive molecules that are not part of the cluster population are part of the "monomeric" diffusive background. From Equation 3, we compute the single-point distribution $P(\delta\rho)$ at steady state, in which $\delta\rho$ is the deviation of the local density from the mean. We find that this distribution is extremely sensitive to the active nature of the filament dynamics; whereas $P(\delta\rho)$ is a Gaussian when $K_d = 0$, as is expected for a thermally agitated brownian particle (inert molecule), it exhibits two significant differences when $K_d > 0$, namely, a broader Gaussian core and exponential tails at both large and small densities (Figure S3Bii). The width of the Gaussian core increases with increasing active temperature T_A. The exponential tails are a direct consequence of $\mathbf{J}_\rho \propto \mathbf{n}$ and the focusing (defocusing) effect of the inward (outward) pointing vectors n. Because the relative contribution to the net aster strength, $\Phi = \int drc\nabla\cdot\mathbf{n}$, is larger for the inward-pointing asters than outward-pointing asters, the tail of $P(\delta\rho)$ is much more prominent at the higher $\delta\rho$ end.

We explored whether these features predicted from the theoretical framework are reflected in the distribution and dynamics of cell surface molecules that couple (as passive molecules, e.g., GPI-APs) or do not couple (as inert molecules, e.g., a short-chain lipid on the outer leaflet) to the dynamic actin filaments (Figure S3).

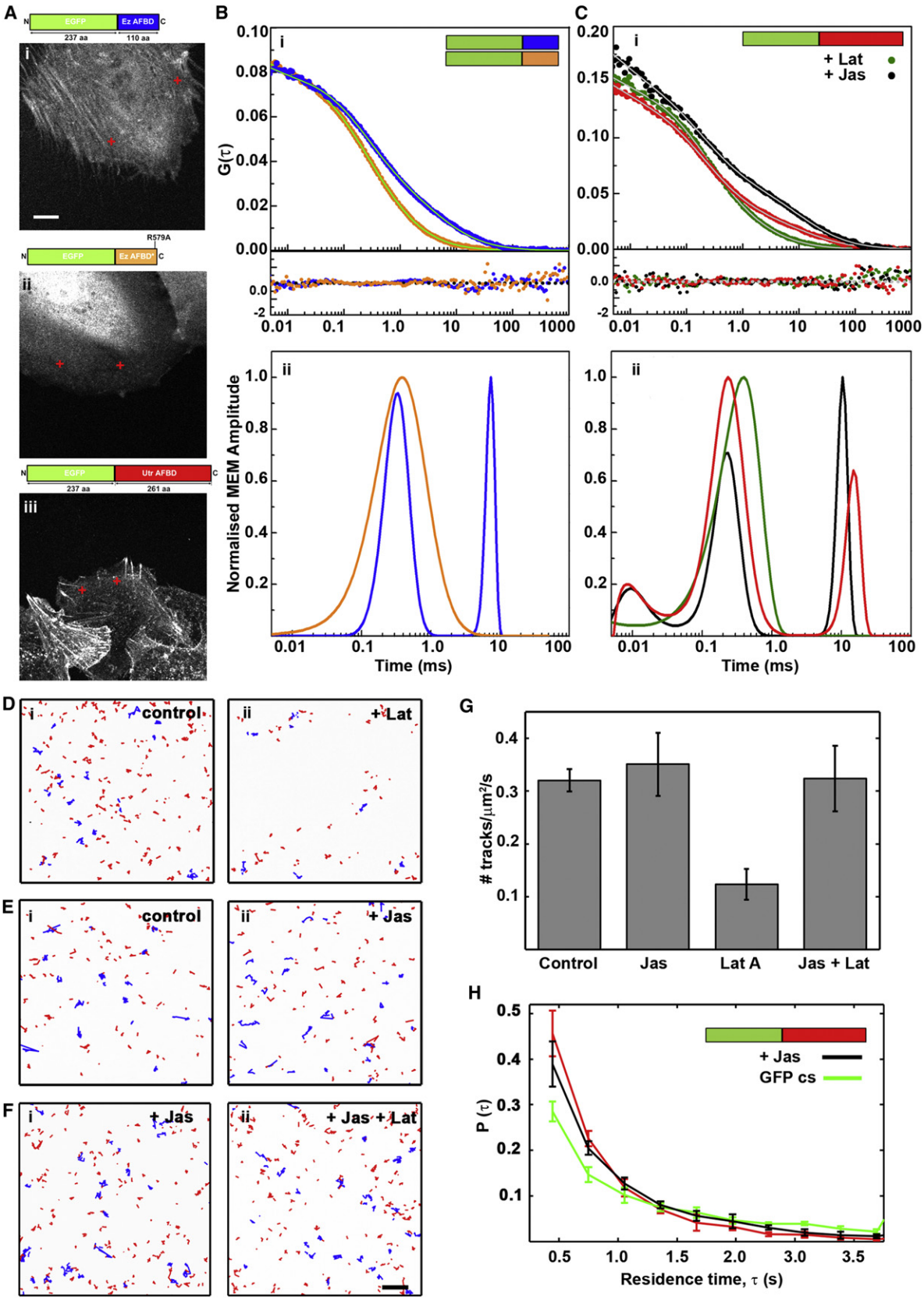
A
N
EGFP
Ez AFBD
C
237 aa
110 aa
i
R579A
N
EGFP
Ez AFBD*
C
ii
N
EGFP
Utr AFBD
C
237 aa
261 aa
iii
B
i
G(τ)
0.10
0.08
0.06
0.04
0.02
0.00
0.0
-2
0.01
0.1
1.0
10
100
1000
ii
Normalised MEM Amplitude
1.0
0.8
0.6
0.4
0.2
0.01
0.1
1.0
10
100
Time (ms)
C
i
+ Lat
+ Jas
0.20
0.15
0.10
0.05
0.00
ii
D
i
control
ii
+ Lat
E
i
control
ii
+ Jas
F
i
+ Jas
ii
+ Jas + Lat
G
tracks/μm²/s
0.4
0.3
0.2
0.1
Control
Jas
Lat A
Jas + Lat
H
P (τ)
0.5
0.4
0.3
0.2
0.1
+ Jas
GFP cs
0.5
1.0
1.5
2.0
3.0
3.5
Residence time, τ (s)

Validation of Theory with Known GPI-AP Distribution Data

To combine the theoretical and experimental data, we need to go from a continuum density description of passive molecules to a discrete particle species description in terms of monomers and nanoclusters (as presented in Theory Section VI, in the Extended Experimental Procedures). We show how every feature of previously performed experiments (Goswami et al., 2008) is qualitatively reproduced here by our theory (Supplemental Information and Figure S3).

The fact that the active parameters entering the dynamical Equations 1 and 2 are sensitive to the actomyosin regulatory machinery and the local distribution of the static cortical filaments immediately implies that the spatial patterning of nanoclusters and the dynamics of diffusion and interconversion rates should exhibit significant heterogeneity, consistent with our FRET observations. Regions enriched in dynamic nanoclusters are associated with a high value of contractility in the active remodeling phase, mirroring the experimental observation (Figure S3A and Supplemental Information).

The single-point distribution of the fluorescence anisotropy of the short-chain 6-((N-(7-nitrobenz-2-oxa-1,3-diazol-4-yl)amino) hexanoyl) sphingosyl phosphocholine (NBD-SM) shows a Gaussian profile, as expected from an inert molecule and consistent with our theory when $K_d = 0$ (see above). In comparison, GPI-APs show a broader Gaussian core and significant exponential tails, exactly as predicted for *passive molecules* (Figure S3B). The width of the Gaussian core decreases and the exponential tails become less pronounced upon perturbations of actin and its actomyosin activity.

The diffusion coefficient of GPI-AP nanoclusters is close to zero. Our theoretical model for passive molecules shows precisely this—nanoclusters, once formed, stay immobilized at the aster core, at most suffering small oscillations about a mean position. Any movement of the passive molecules constituting the nanocluster occurs largely as a consequence of fragmentation of a nanocluster into monomers.

The remodeling dynamics of the actin asters in regions II and III (Figures 2A and 2B) results in the fragmentation-formation dynamics of the nanoclusters, from which we compute the probability distribution of fragmentation and aggregation rates. This allows us to display an "Arrhenius plot" of the ratio of the mean fragmentation to aggregation rates versus $1/T_A$, the activity temperature. The overall nonmonotonic behavior, the flatness of the curve at high activity, and the sharp fall at the transition are precisely the features present in the Arrhenius plot computed from our analysis of the recovery of the FRET anisotropy and intensity after photobleaching (Figure S3C). In addition, we predict significant changes upon perturbation of both actin and its actomyosin activity, again consistent with our experimental observations.

A salient observation from our earlier FRET analysis is that the mean anisotropy over the entire cell is independent of intensity, a relation that holds even for a large enough patch on the cell surface (Sharma et al., 2004). This implies that, over large scales, the fraction of GPI-APs in nanoclusters is independent of total number of GPI-APs. However, when measured over smaller scales, we find that the anisotropy initially decreases and then crosses over to the same intensity-independent value at higher intensities. Our theory reproduces this unusual feature for passive molecules by showing that the fraction in nanoclusters is independent of the total number when the number of passive molecules is large (Figure S3D). This trend cannot continue for purely passive molecules, and the fraction in nanoclusters should eventually decrease at very high concentration. We may not have achieved high enough expression levels to observe this regime in experiments. Alternatively, GPI-APs at high concentrations might behave as active particles for which the trend would continue at higher expression levels (see also Theory Section III in the Extended Experimental Procedures).

In summary, our theoretical framework invoking dynamic actin filaments in conjunction with motor activity provides a consistent explanation of *all* of the observations of the distribution and dynamics of passive and inert molecules on the plasma membrane from previously published experimental data of Goswami et al. (2008).

Testing the Basic Assumptions for Existence of Short Cortical Dynamic Actin

We next tested the key assumptions of the model, namely the presence of dynamic actin filaments underlying the plasma membrane. To study the dynamics of actin we utilized two methods, fluorescence correlation spectroscopy (FCS) and single-molecule-based particle tracking (SMPT). Both of these

Figure 3. Probing the Dynamics of Cortical Actin Filaments

(A) Schematic of the three GFP-tagged actin-filament-binding domains (AFBDs) overlaid on typical confocal images of cells expressing these proteins. FCS data were collected from typical regions at the cell periphery as indicated (+). AFBD* corresponds to the R579A mutant in the Ez-AFBD that abolishes actin binding. Scale bar, 10 μm.

(B and C) Graphs show autocorrelation decays and respective fits (green line) and residuals (bottom) (i) as well as corresponding distributions of diffusion timescales (ii) obtained from maximum entropy method (MEM) analysis of the FCS data for the indicated constructs. GFP-Ez-AFBD (B; blue symbols), GFP-Ez-AFBD* (B; orange symbols), and GFP-Utr-AFBD (C) were expressed in CHO cells in the absence (C, red symbols) or presence of latrunculin A (Lat, 4 μM; green symbol) or jasplakinolide (Jas, 2 μM; black symbol). Note the presence of fast and slow diffusion timescales of GFP-Ez-AFBD and GFP-Utr-AFBD and the absence of the latter in GFP-Ez-AFBD* and LatA-treated GFP-Utr-AFBD-expressing cells.

(D–F) Tracks of single molecules of GFP-Utr-AFBD expressed in AGS cells, collected using a TIRF set up at a frame rate of 7 fps before adding any drugs or after the addition of latrunculin A (Lat, 2 μM) or jasplakinolide (Jas, 1 μM) or both, as indicated. The tracks are color coded by their residence times, with the blue tracks being those with $\tau > 1.5$ s.

(G) Plot shows the number of tracks per $\mu m^2/s$ for the treatments, as indicated. Error bars indicate SD.

(H) Graphs show the distribution of residence times for SM in the TIRF field for the different treatments, as indicated. The distribution of residence times (τ) of single molecules of GFP adhered to a coverslip (GFPcs) were obtained by imaging under the same conditions as GFP-Utr-AFBD expressed in cells. Error bars indicate SD. Scale bar, 1.5 μm.

See also Figure S4, Table S1, and Movies S1–S3.

techniques require us to utilize a fluorescent probe that best reports on the dynamics of actin filaments. We first studied the dynamics of GFP-tagged actin (GFP-actin) by FCS. This turned out not to be a viable probe, as the FCS measurement simply gave us a single correlation time (τ = 0.3 ms; data not shown), consistent with monomer diffusion for GFP-actin. This was presumably due to the presence of a large monomer pool of actin in the cell and the low labeling densities necessary for FCS measurements.

We next turned to GFP-tagged actin filament-binding domains (GFP-AFBDs) derived from Ezrin (Saleh et al., 2009; GFP-Ez-AFBD) and Utrophin (Burkel et al., 2007; GFP-Utr-AFBD) as probes (Figure 3A). In each case, we were able to detect at least two diffusing species (Figures 3B and 3C and Table S1), one corresponding to the diffusion of the GFP-AFBD monomer ($\tau \approx$ 0.25 ms) and another to a much longer diffusion timescale ($\tau \approx$ 10 ms). The slower diffusing species arises from the association of GFP-AFBD with an actin filament, as it is abolished either when the actin filament-binding domain (in the Ez-AFBD) is mutated (Figure 3B) or when actin polymerization is inhibited by the addition of latrunculin right before the FCS measurement (Figure 3C). In addition, on application of jasplakinolide, a filament-stabilizing agent (Bubb et al., 1994), we find no significant difference in the diffusion timescales of the GFP-Utr-AFBD (Figure 3C). Furthermore, these timescales are not a result of binding and unbinding kinetics of the GFP-AFBDs from actin filaments, as we detect similar diffusion times for GFP-Ez-AFBD and GFP-Utr-AFBD, although FRAP measurements show that these GFP-AFBD have very different dissociation rates from stable actin filaments (Figure S4A; Burkel et al., 2007).

We estimate the typical actin filament length from the FCS data (Figure 3) to be $\approx$ 250 nm; admittedly, this estimate is crude (Extended Experimental Procedures). Although the measurement of the length distribution of these dynamic actin filaments requires a more detailed analysis, these results are consistent with the existence of a rapidly diffusing filamentous actin species at or near the membrane.

We next focus on a region that is immediately adjacent to the inner leaflet of the PM and study the dynamics of the GFP-ABFDs using a TIRF-based SMPT approach. In this assay, a single-fluorescent molecule (SM) associated with a slowly turning over filamentous structure will be visualized as a puncta that may be tracked using SMPT routines (Jaqaman et al., 2008). We chose GFP-Utr-AFBD as the probe because it has a low off rate from actin filaments (timescale > 10 s; Figure S4A), which gives us the best chance to follow the dynamics of filament-bound GFP-Utr-AFBD at the frame rate $\approx$ 100 ms (Movies S1, S2, and S3). These punctae, representing SMs of GFP (Figure S4C), are tracked in consecutive frames (Figures 3D–3F) to obtain a distribution of residence times τ that the SM remains in the field of view (Figure 3H). From our analysis of the trajectory of many SMs, as well as their response to specific actin perturbations, we make three observations. First, the majority of the SMs have a residence time that is shorter than the photobleaching time of GFP molecules immobilized on a coverslip (Figure 3H), implying that either the structures that they are associated with are rapidly turning over or they are rapidly diffusing away from the field of view. Second, the SMs disappear within 4–5 s of applying latrunculin (Movie S2 and Figures 3D and 3G), whereas they are stabilized by the application of jasplakinolide (Figure 3E, G) and consequently become resistant to latrunculin treatment (Movie S3 and Figure 3F). Third, during their localization at the membrane, GFP-Utr-AFBD appear to move over very short distances, about $\approx$ 100 nm, not significantly different from SM of GFP adhered to coverslip dishes (Figure S4D).

These results provide compelling evidence for the existence of short dynamic actin filaments at the inner leaflet of the cell membrane, verifying key assumptions of our theoretical model.

Verification of Additional Predictions of Dynamic-Actin-Coupled Behavior

From the agreement between theory and experiments reported so far, it appears that GPI-APs are passive molecules and thus act as reporter particles for the existence and patterning of the dynamic actin filaments at the cortical aspect of the membrane. Our model makes two experimentally verifiable predictions: (1) anomalous number fluctuations exist as a feature of the dynamics of reporter particles that reflects the active dynamics of underlying actin filaments, and (2) any cell surface molecule constructed to bind directly to F-actin will form actin-dependent nanoclusters with properties similar to the GPI-AP nanoclusters.

Because passive molecules are actively driven by their binding to the polar filaments, the statistics of orientational fluctuations should affect the equal time density or number fluctuations of the passive molecule. Here, number fluctuations refer to deviations in the instantaneous number of molecules in a given area compared to the time-averaged number in the same area. Our model predicts that, in regimes in which the mean filament orientation is nonzero at large scales, number fluctuations of passive molecules are much more than what is expected of a brownian particle (inert molecule) in thermal equilibrium (see Theory Section IV in the Extended Experimental Procedures). These enhanced fluctuations are obvious to the eye (snapshot in Figure S3A); in addition, the significant exponential tails in the single-point distribution (Figure S3B) are indicative of the same. To quantitate these large fluctuations, we compute the mean $\overline{N}$ and root-mean-square (rms) deviations $\Delta N \equiv \sqrt{\delta N^2}$ of the number of molecules N in a region of size L. For any thermal equilibrium system with a finite compressibility, the number fluctuations will scale as $\Delta N \propto \sqrt{\overline{N}}$. To obtain the number fluctuations of the passive molecules, we note that active (advective) transport dominates over the slower diffusive transport at large spatial scales L, which implies that both $\mathbf{J}_c$ and $\mathbf{J}_\rho \propto \mathbf{n}$. Thus, fluctuations of the orientation $\boldsymbol{n}$ will drive particle currents and hence fluctuations in the passive particle density. This implies that the number fluctuations are enormous; the rms fluctuations $\Delta N \propto N^{4/5} = N^{0.8} > N^{0.5}$ (see discussion in Theory Section IV in Extended Experimental Procedures). This value of the anomalous exponent, viz. 0.8, is valid when the actin configurations possess a net orientation $\langle c\, \mathbf{n}\cdot\mathbf{x}\rangle$; as noted earlier, this is true in the remodeling regimes. We return to this point in the Discussion. On setting $K_d = 0$ in (3), i.e., when the cell surface molecule does not bind to the active actin, we recover the usual brownian particle $\sqrt{N}$ fluctuations.

Note that, in practice, the passive molecules are subject to *both* active and thermal noise; the former dominates at larger values of N. Thus for a passive molecule, we would expect that the number fluctuations exhibit a crossover from a $\sqrt{N}$ behavior to the anomalous $N^{0.8}$ behavior as N increases. This value of N at which the crossover occurs depends on the strength of the activity and would increase with decreasing activity.

In fluorescence experiments, we can measure the mean number and its fluctuations by measuring the mean intensity and intensity fluctuations. We thus measure the intensity fluctuations from the fluorescent molecules on the plasma membrane over increasing sampling area (Figure 4A and inset), which allows us to obtain the relationship between ΔN and $\sqrt{N}$ (Figure 4B). The intensity fluctuations of fluorescein in solution and short-chain lipids N-(4,4-difluoro-5,7-dimethyl-4-bora-3a,4a-6 diaza-s-indacene)-3-pentanoyl sphingosylphosphocholine (BODIPY-C5-SM) on the cell membrane show the usual $\sqrt{N}$ dependence, as expected of a brownian particle (Figure 4B, blue circles). In contrast, our candidate passive molecules GFP-GPI (Figure 4B, red circles) and folate receptor (FR-GPI) (Figures 4C and 4D, red circles) show enhanced fluctuations at large N, in qualitative agreement with our theoretical predictions; the $\Delta N \propto N^{0.8}$ arising from phase fluctuations of the orientation is displayed for comparison. The crossover from $\sqrt{N}$ fluctuations at smaller N to the anomalous fluctuations at larger N, as discussed above, is apparent in Figures 4C and 4D (red circles). As noted above, the crossover value of N must change with activity; to check this, we reduce both actin dynamics and nonmuscle myosin 2 motor activity by adding titrated amounts of latrunculin A, jasplakinolide, and blebbistatin (see Extended Experimental Procedures and Figure S5). Consistent with our predictions, the crossover to the anomalous fluctuations consistently occurs at larger N (Figure 4C, i and ii, blue circles and bars) when actomyosin activity is reduced. A similar loss in anomalous fluctuations is observed when cholesterol levels are perturbed by extraction with methyl-β-cyclodextrin (Figure 4D, i and ii, green circles and bars).

To test whether a membrane protein that acquires the capacity to bind actin will form nanoclusters, we constructed model transmembrane proteins (Figure 5A) that have extracellular reporter domains and cytoplasmic domains with an AFBD (FRTM-Ez-AFBD) or a mutated version of AFBD that cannot bind actin (FRTM-Ez-AFBD*), and we explored their steady-state organization in live cells. Steady-state anisotropy measurements on the fluorescent folate-labeled model proteins show that only the protein with the intact actin-binding domain exhibits homo-FRET, consistent with the formation of nanoclusters similar to GPI-APs (Figures 5B–5D, blue circles). In contrast, neither FRTM-Ez-AFBD* (Figure 5B-D; red circles), which cannot bind to actin, nor FRTM-Ez-AFBD on blebs derived from Lat A-treated cells (Figure 5C; green circles) form nanoclusters, as determined from their steady-state anisotropy and photobleaching profile.

To strengthen these observations, we directly measure inter-protein distances using time-resolved anisotropy decays (Figure 5E) of mEGFP-fusion proteins (GFPTM-Ez -AFBD and GFPTM-Ez-AFBD*) expressed in cells (Figure 5F). Picosecond time-resolved fluorescence emission anisotropy decays of GFPTM-Ez-AFBD exhibit a fast and a slow decay component, similar to GFP-GPI (Figure 5G and Table 1). The fast decay is due to homoFRET between mEGFP molecules and corresponds to an interprotein distance of ~3 nm, whereas the slow component is due to the rotational relaxation of the mEGFP moiety (Sharma et al., 2004). This fast component is absent in GFPTM-Ez-AFBD located on membrane blebs and in the actin-binding mutant GFPTM-Ez-AFBD* (Figures 5G and 5H and Table 1).

These results verify two distinctive predictions of our theoretical model—namely, the existence of anomalous number fluctuations (and their disappearance when the coupling to cortical actin is perturbed) and the generalization of the features of nanoclustering to cell surface proteins that directly couple to actin.

DISCUSSION

An Active Model for Membrane Component Organization Mediated by Dynamic Cortical Actin

The key ingredients of the active composite model of the membrane that we present here are the presence of two species of actin (a dynamic treadmilling actin filament population embedded within a relatively stable actin mesh) at the cell cortex and the model's capacity to engage with motor activity and membrane composition. The dynamics of motor-driven actin filaments naturally give rise to an elaborate patterning of actin filaments in the form of collections of asters (Figure 2; see also Gowrishankar, 2009; K.G. and M.R., unpublished data). The inevitable noise arising from the stochasticity of motor activity dynamically remodels these asters. This patterning of the dynamic actin filaments depends on a host of regulatory proteins and the spatial distribution of the static meshwork, suggesting that regions that are enriched (or depleted) in dynamic asters are heterogeneously distributed on the cell surface.

The coupling of dynamic actin to cell surface molecules suggests a classification—namely, inert, passive, and active molecules. Here, we have provided evidence for the distinctive features of the spatiotemporal organization of inert (e.g., short-chain lipids) and passive (e.g., GPI-APs and transmembrane protein with an actin-binding domain) molecules on the cell surface, which are driven to form transient nanoclusters by configurations of the dynamic actin. This could represent a very general mechanism of creating a regulated molecular scale complex in the membrane of cells in conjunction with the local actin architecture. Though we discuss below how outer leaflet lipids may connect to cytoplasmic actin, some inner leaflet lipids and many cell surface proteins can directly connect to the cytoplasmic actin using a number of actin-binding motifs (Gimona et al., 2002; Saarikangas et al., 2010). Of course, indirect coupling via regulatable protein-protein interaction motifs such as PDZ, SH3 (Src-homology domain 3), or PRD (proline-rich domain) offer further interaction possibilities, covering a large range of cell surface proteins.

Active cell surface molecules (which we do not study here) represent cell surface molecules that are capable of interacting with actin and modifying its dynamics; these molecules have the capacity to influence their local environment by being able to switch "on" their activity. Prime examples of such active molecules are integrins and T cell receptors, which not only recruit molecules involved in actin cytoskeleton modification

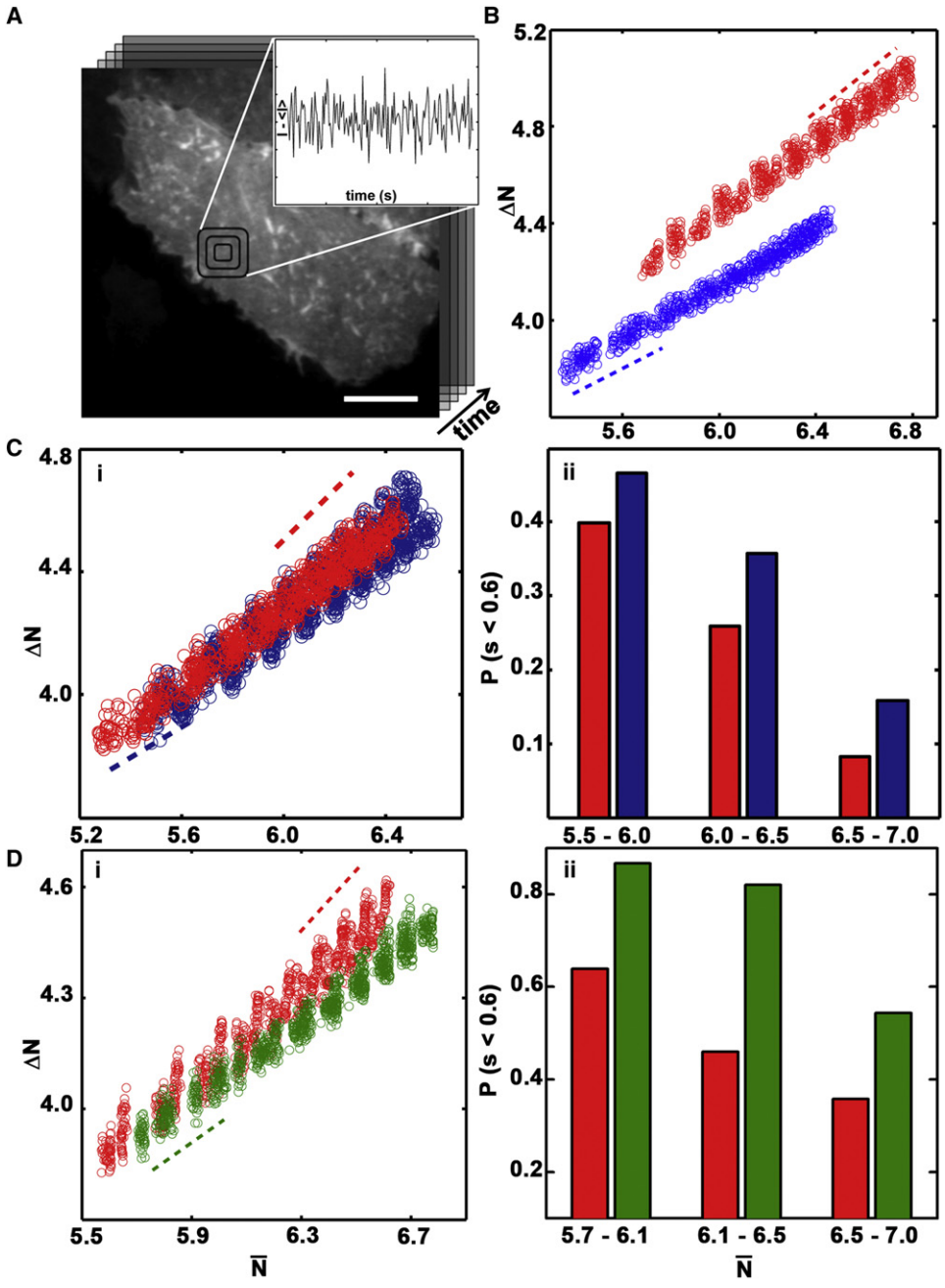

Figure 4. Anomalous Number Fluctuations of GPI-AP: Comparison of Passive and Inert Molecules

(A) Schematic representation of fluorescence intensity measurements made from areas (boxes) of increasing size (8 × 8 to 24 × 24 pixels) chosen from flat regions on the cell surface (Extended Experimental Procedures). The intensity is integrated over a specific box size as indicated, as a function of time, and after correction for photobleaching, plotted to show the fluctuations of the intensity about the mean (inset). $I \propto N$; this is equivalent to generating the time series of the total number of fluorescent molecules in each box.

(B) Log-log plot of rms number (or equivalently intensity) fluctuations ΔN versus mean number $\overline{N}$ of molecules in a patch of the plasma membrane (detailed in the Extended Experimental Procedures). The inert short-chain lipid, BODIPY-SM (blue dots), shows a slope 0.5 (blue dashed line). On the other hand, GFP-GPI (red dots) shows a significantly larger slope. For passive molecules, the theory suggests that $\Delta N \propto \overline{N}^{4/5}$, implying a slope of 0.8 (red dashed line).

(C and D) Similar anomalous fluctuations for another GPI-AP, the FR-GPI (red) acquired over flat regions of different cells show a crossover with a slope ~0.5 for smaller intensities to a slope ~0.8 for larger intensities. For inert molecules, the slope remains at 0.5 for all intensities. For cells (n = 8) perturbed with titrated quantities of blebbistatin, latrunculin, and jasplakinolide (C, blue; Extended Experimental Procedures) or subjected to cholesterol depletion (D, green), the crossover to the anomalous $\overline{N}^{0.8}$ scaling happens at larger intensities. This is highlighted by comparing the fraction of curves that have slopes below 0.6 for three different ranges in intensity, for the wild-type (red) and perturbations (blue, green).

See also Figure S5.

upon activation, but are also organized in microclusters by actin-dependent processes (Kaizuka et al., 2007; van Zanten et al., 2009; Varma et al., 2006; Yu et al., 2011).

Dynamic Cortical Actin Can Have Polar or Apolar Organization

The most important consequence of our model of the active composite membrane is in actively bringing together passive cell surface molecules at different scales, ranging from the nanoscale to the mesoscale. As mentioned above, this could be achieved either by having active polar filaments organized with polar order (described by an orientation vector n) or with apolar order (described by an orientation tensor **Q**). For clarity, we restricted our discussion to active polar organization and the consequent aster patterns as the actively regulatable focusing regions. However, qualitatively similar features are obtained when passive molecules are driven by filaments organized in an *apolar* manner (Chaudhuri et al., 2011). For instance, a meshwork of dynamically turning over actin filaments with transient crosslinkers such as myosin can serve as a template on which passive molecules may bind and unbind. Upon motor activity, the meshwork may locally deform, creating transient zones that are capable of bringing together the bound passive molecules. Mathematically, this active deformation of the mesh will result in an active advective current $\mathbf{J}_c \propto \rho \nabla \cdot (c\mathbf{Q})$ rather than $\mathbf{J}_c \propto \rho\, \mathbf{n}$ in (3). The qualitative features that result will be the same as in the polar case. However, the value of the exponent describing the anomalous number fluctuations, 0.8 in this case, is specific to the model with polar order. This value would change if the filaments are organized in an apolar manner, although it would still be significantly larger than 0.5 (expected for thermally driven fluctuations). Given the errors inherent in the experiments, this would still be consistent with our experiments.

GPI-APs as Passive Particles

For GPI-APs to behave as passive molecules, the outer leaflet lipid-anchored GPI-AP must interact, albeit indirectly, with the actin at the inner leaflet. There is evidence for such a transbilayer link, involving cholesterol, sphingolipids, and PIPs, to elements of the actin machinery at the inner leaflet, coming from studies on single-particle tracking on cells (Dietrich et al., 2002; Suzuki et al., 2007). Studies from computer simulations (A. Polley, S.M., and M.R., unpublished data) and artificial membranes (Wan et al., 2008) suggest a transbilayer link between GPI-APs and inner leaflet lipids, involving long-chain saturated lipids and cholesterol in a local liquid-ordered (l_o) environment. This, coupled with active driving by the dynamic actin filaments, is sufficient to capture every feature of the organization and dynamics of GPI-APs. We stress that "equilibrium" mechanisms of molecular clustering, including the presence of a clustering scaffold, are not consistent with the entire set of experimental results on the GPI-AP organization on the cell surface (see Theory Section V in Extended Experimental Procedures). Indeed many experimental observations, including those on the formation and retraction of cellular blebs, suggest that, as soon as the sources of cortical activity are removed or if cholesterol is removed, the GPI-APs behave as inert molecules (similar to exogenously added short-chain lipids).

Active Cortical Actin and Its Regulators

From our FCS experiments, it appears that there is a significant population of dynamic actin filaments whose lengths are distributed about 250 nm. For our polar model to be applicable at the scale of nanoclusters, the length of the dynamic actin filaments should be smaller than the distance between asters. Recent NSOM studies of GPI-AP nanoclusters on resting monocytes (van Zanten et al., 2009) indicate a mean intercluster distance around 250 nm, which puts a rough upper bound on the filament size, consistent with our FCS data. Short filamentous actin has been observed at or close to the PM (Cao et al., 1993; Spudich et al., 1988), and more recently, its generation by the action of cofilin and its utilization at endocytic sites have been proposed (Okreglak and Drubin, 2010). These data suggest that short oligomeric actin is a necessary byproduct of the growth and remodeling dynamics of the actin meshwork and is required for maintaining a dynamic actin meshwork apposed to a stationary flat membrane surface.

Our FCS and SMPT experiments support the assumptions of a rapidly turning over pool of dynamic actin filaments in the vicinity of the membrane. The SMPT measurements also indicate that dynamic filaments are recruited to a narrow region (<100 nm) at the cell membrane and exhibit turnover kinetics similar to nanocluster disassembly reported earlier (Goswami et al., 2008).

In addition, the model requires a molecular mechanism for active contractility, consistent with a role for a myosin or myosin-like activity. Evidence for this comes from two types of experiments—the first in which application of blebbistatin, a specific inhibitor of myosin 2, inhibits the formation and fragmentation dynamics of the GPI-AP nanoclusters, both in flat membranes and in retracting blebs (Goswami et al., 2008), and the second in which the addition of inhibitors of actin and myosin activity serves to restore the intensity fluctuations to those expected from a brownian particle (as shown here).

Actively Regulatable Membrane Domains

In a logical extension of our theory, we suggest that passive molecules that exhibit differential ability to couple with the dynamic filaments (via on and off rates) or exhibit weak attractive interactions between each other are capable of segregating into separate clusters and thereby forming separate domains (A. Chaudhuri, S.M., and M.R., unpublished data).

The ability of the cell to locally regulate the construction and dissipation of the nanocluster platforms and hence local membrane composition in the face of thermal noise may be the key to the construction of regulatable microdomains (active rafts) in cell membranes. This also provides a powerful mechanism for the sorting of membrane components, as well as conferring spatiotemporal regulation of chemical reactions mediated by substrates that are subjected to active cytoskeletal remodeling (Chaudhuri et al., 2011). These active domains may serve as sites for membrane deformation, such as the formation of endocytic buds or secretory vesicles, either because they have actively segregated molecular components that might favor

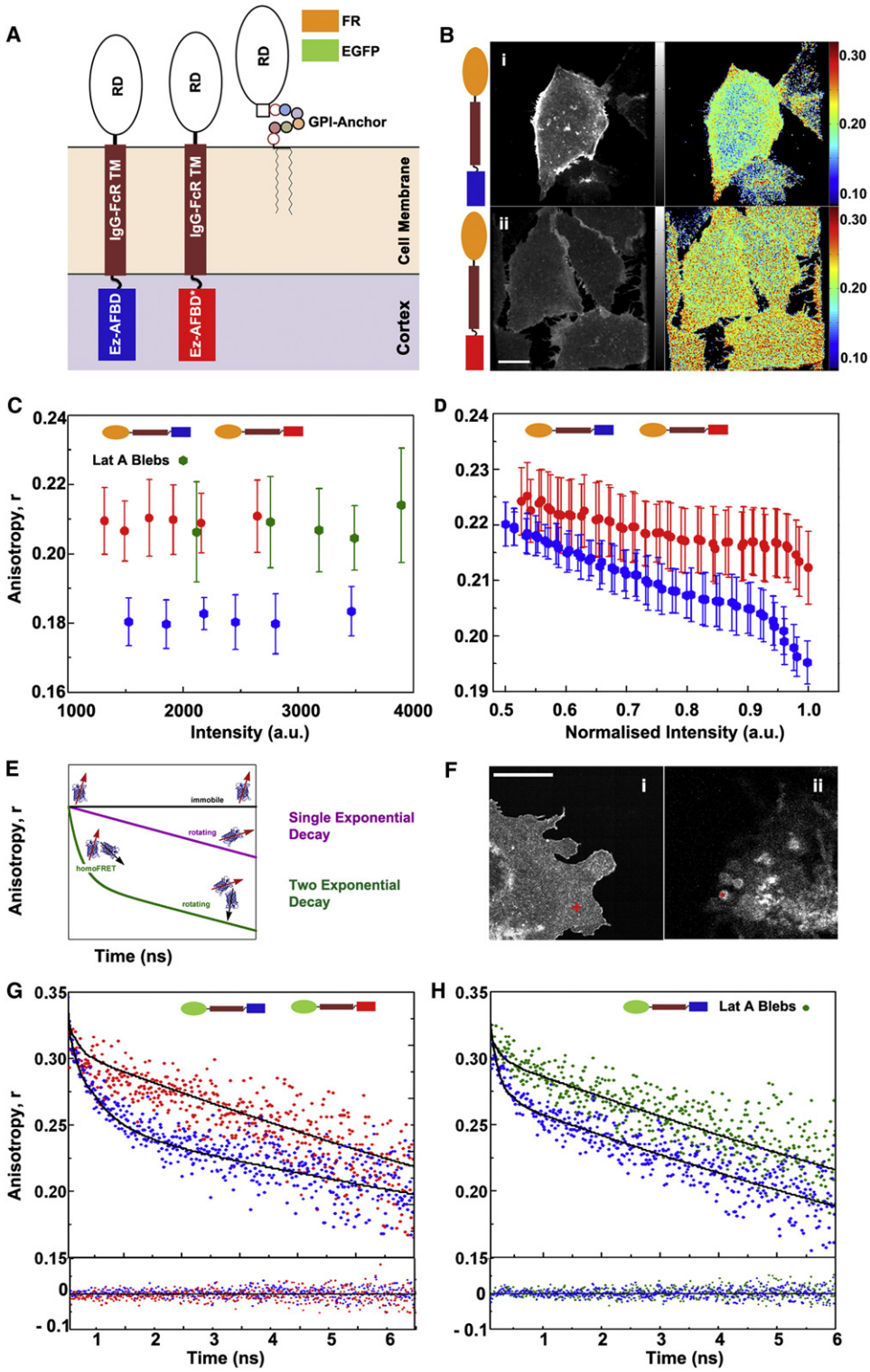

Figure 5. Actin Binding at the Cytoplasmic Leaflet Induces A Model Transmembrane Protein To Form Nanoclusters

(A) Schematic of the location of AFBD in model transmembrane proteins constructed from the fusion of N-terminal receptor domains (RD), the folate receptor (FR), or mEGFP (GFP) to a transmembrane domain and then to the C-terminal domain of Ezrin (Ez-AFBD) or a mutated version of the same, ezrin-R579A (Ez-AFBD*). Note the possibility of a direct link with cytoplasmic actin filaments in RDTM-Ez-AFBD, but not in RDTM-Ez-AFBD*.

(B) Intensity and steady-state anisotropy images of FRTM-Ez-AFBD and FRTM-Ez-AFBD* were obtained from PLB-labeled cells expressing the respective proteins and imaged on a spinning disk confocal microscope.

Table 1. Time-Resolved Anisotropy Measurements

Fusion Protein (Treatments/Locations)	n	r_0	τ_1 (ns)	A_1	τ_2 (ns)	A_2	r_{ss}	χ^2
GFPTM-Ez-AFBD (control/flat regions)	8	0.4 (±0.01)	0.49 (±0.2)	0.12 (±0.05)	37.8 (±13)	0.88 (±0.05)	0.34 (±0.03)	1.06
GFPTM-Ez-AFBD* (control/flat regions)	9	0.41 (±0.01)	24 (±3)	1			0.37 (±0.02)	1.15
GFPTM-Ez-AFBD (Lat A 20μm / Bleb)	5	0.39 (±0.01)	27 (±3)	1			0.36 (±0.01)	1.25
mGFP-GPI (control/flat regions)	9	0.4 (±0.01)	0.45 (±0.24)	0.08 (±0.02)	34 (±3)	0.92 (±0.02)	0.35 (±0.01)	1.05
mGFP-GPI (Saponin 0.2% / flat regions)	8	0.41 (±0.01)	25 (±3)	1			0.38 (±0.01)	1.05

Time-resolved anisotropy measurements were carried out as detailed in the Extended Experimental Procedures. n = number of independent measurements; r_0 = fundamental anisotropy; $\tau_{1,2}$ = anisotropy decay timescales; $A_{1,2}$ = amplitudes of anisotropy decay components; r_{ss} = steady-state anisotropy; χ^2 = average chi-square (variation across independent measurements < 10%). Values in parentheses indicate SD.

budding or as a direct consequence of the lateral stresses on the membrane due to actomyosin contractility. These different phenotypic outcomes can be realized by locally tuning cortical activity, such as motor contractility or actin (de)polymerization, and suggest that the cell might have local control of membrane properties for specific function.

EXPERIMENTAL PROCEDURES

Dynamics of Actin Filaments and Passive Molecules

Equations 1, 2, and 3 were discretized on a grid with spacings ($\Delta x = \Delta y = 0.2$, in units of L_p). The size of the patch L = 200,500,… (in units of L_p) is taken to be much larger than the length scales L_p, L_b, and L_s. The equations were numerically evolved in time steps of $\Delta t = 0.05$ in units of the advection time (L_p/v_0), using an implicit operator splitting method (Press et al., 2007), stable up to second order in time. Periodic, reflecting (filaments perpendicular to the wall), and parallel (filaments parallel to the wall) boundary conditions were employed. Comparisons with experiments were made by converting the passive particle density into maps of numbers of clusters and monomers (see Theory Section VI in the Extended Experimental Procedures). The numerical values of the parameters chosen in the calculations are listed in Theory Section VII in the Extended Experimental Procedures.

Plasmids, Cell Labeling, and Imaging

All plasmids and constructs were obtained or generated as detailed in the Extended Experimental Procedures. Chinese hamster ovary (CHO) cell lines expressing either GPI-anchored GFP (GFP-GPI) or folate receptor (FR-GPI) or their transmembrane variants were maintained in folic acid-free Ham's F12 medium and imaged directly (GFP-GPI) or labeled with a fluorescent folate analog, PLB (pteroyl-lysine conjugated to BODIPY-TMR), and prepared for imaging as described (Goswami et al., 2008). Folate-receptor-expressing human gastric cell line AGS (FRAGS) was generated by stable transfection of human folate receptor (FR-GPI) and maintained in folic acid-free Ham's F12 medium containing 50 μg/ml Hygromycin. Cells were labeled with the short-chain BODIPY C_5-SM analog as detailed (Goswami et al., 2008). To observe the effect of the actin or myosin inhibitors, after labeling the cells with PLB, the inhibitors were added into the imaging buffer at the indicated concentrations.

The labeled cells were also imaged using total internal reflection fluorescence microscopy (TIRF) at 37°C, and images were collected on a customized Nikon TE2000E microscope (Ghosh et al., 2012). To obtain the intensity fluctuations, images (200 ms exposure) were acquired every 2 s. The total fluorescence intensity was measured from regions of interest, with areas ranging from 0.6 × 0.6 to 2 × 2 μm^2, corrected for bleaching effects and plotted against time. The standard deviation of the time trace was plotted on a log-log scale against the mean intensity. This graph was fitted to a linear regression to obtain the slope. Fluorescein or BODIPY TMR dye solutions in water were diluted to give a similar intensity range as the labeled cells, imaged and analyzed exactly as above.

Steady State-Anisotropy Measurements

Cells were labeled with PLB and imaged using a spinning disk confocal system (Andor Technologies, Belfast, Northern Ireland) custom adapted for fluorescence emission anisotropy (Ghosh et al., 2012). The labeled cells were excited with 561 nm laser illumination, after which parallel and perpendicular polarized fluorescence emission was resolved by passing the emission through a polarizing beam splitter and collected using two EMCCD detectors. Image processing, analysis, and quantification were performed using Metamorph 7.0 software (Molecular Devices Corporation, CA, USA) as described (Goswami et al., 2008; Sharma et al., 2004).

SUPPLEMENTAL INFORMATION

Supplemental Information includes Extended Experimental Procedures, five figures, two tables, and three movies and can be found with this article online at doi:10.1016/j.cell.2012.05.008.

ACKNOWLEDGMENTS

We thank S. Ramaswamy and J. Toner for critical reading of the manuscript and Drs. Thomas Lecuit, Helen Morrison, and Antonio Sechi for their generous gifts of the actin-binding constructs. We thank P. Srivastava and K. Hussain for

(C) Fluorescence anisotropy of cells expressing FRTM-Ez-AFBD (blue circle) and FRTM-Ez-AFBD* (red circle) against fluorescence intensity, derived from at least 100 regions across 8–10 cells. Fluorescence anisotropy of FRTM-Ez-AFBD is concentration independent and highly depolarized compared to FRTM-Ez-AFBD*, resembling FRTM-Ez-AFBD in membrane blebs (green circle, n = 50) generated by LatA treatment to disrupt the actin cytoskeleton. Error bars indicate SD.
(D) Graph shows the extent of change of emission anisotropy upon photobleaching FRTM-Ez-AFBD, but not FRTM-Ez-AFBD*, consistent with homo-FRET in the former. Error bars indicate SD.
(E) Schematic (adapted from Altman et al., 2007) depicting the time-resolved anisotropy decays from GFP molecules in different configurations.
(F) Multiphoton images of GFPTM-Ez-AFBD-expressing cells treated with LatA 20 μM on flat regions (+) and blebs (*) where anisotropy decay measurements were conducted.
(G and H) Single-point time-resolved anisotropy decay measurements were carried out using multiphoton excitation at 37°C. Graphs show anisotropy decay profiles (filled circles), their corresponding fits (black lines) and residuals (bottom) obtained from CHO cells expressing GFPTM-Ez-AFBD (G and H, blue) or GFP-Ez-AFBD* (G, red) from flat regions or from blebs produced in cells expressing GFPTM-Ez-AFBD upon LatA treatment (20 μM). Anisotropy decay profiles from GFPTM-Ez-AFBD* and GFPTM-Ez-AFBD on blebs lack the fast decay component present in cells expressing GFPTM-Ez-AFBD (Table 1), confirming that the actin-binding mutant proteins do not form nanoclusters. Scale bar, 10 μM.

help in quantifying the FCS data, Balaji Ramalingam for help with SMPT, and the Central Imaging Facility at NCBS. M.R. acknowledges grants from CEFIPRA (3504-2) and HFSP, and S.M. acknowledges support from a JC Bose fellowship from the DST.

Received: August 19, 2010
Revised: October 3, 2011
Accepted: May 8, 2012
Published: June 7, 2012

REFERENCES

Altman, D., Goswami, D., Hasson, T., Spudich, J.A., and Mayor, S. (2007). Precise positioning of myosin VI on endocytic vesicles in vivo. PLoS Biol. *5*, e210.

Backouche, F., Haviv, L., Groswasser, D., and Bernheim-Groswasser, A. (2006). Active gels: dynamics of patterning and self-organization. Phys. Biol. *3*, 264–273.

Bubb, M.R., Senderowicz, A.M., Sausville, E.A., Duncan, K.L., and Korn, E.D. (1994). Jasplakinolide, a cytotoxic natural product, induces actin polymerization and competitively inhibits the binding of phalloidin to F-actin. J. Biol. Chem. *269*, 14869–14871.

Burkel, B.M., von Dassow, G., and Bement, W.M. (2007). Versatile fluorescent probes for actin filaments based on the actin-binding domain of utrophin. Cell Motil. Cytoskeleton *64*, 822–832.

Cao, L.G., Fishkind, D.J., and Wang, Y.L. (1993). Localization and dynamics of nonfilamentous actin in cultured cells. J. Cell Biol. *123*, 173–181.

Chaudhuri, A., Bhattacharya, B., Gowrishankar, K., Mayor, S., and Rao, M. (2011). Spatiotemporal regulation of chemical reactions by active cytoskeletal remodeling. Proc. Natl. Acad. Sci. USA *108*, 14825–14830.

de Gennes, P.G., and Prost, J. (1993). The Physics of Liquid Crystals (Oxford, UK: Clarendon Press).

Dietrich, C., Yang, B., Fujiwara, T., Kusumi, A., and Jacobson, K. (2002). Relationship of lipid rafts to transient confinement zones detected by single particle tracking. Biophys. J. *82*, 274–284.

Edidin, M. (2003). The state of lipid rafts: from model membranes to cells. Annu. Rev. Biophys. Biomol. Struct. *32*, 257–283.

Fujita, A., Cheng, J., Hirakawa, M., Furukawa, K., Kusunoki, S., and Fujimoto, T. (2007). Gangliosides GM1 and GM3 in the living cell membrane form clusters susceptible to cholesterol depletion and chilling. Mol. Biol. Cell *18*, 2112–2122.

Fujiwara, T., Ritchie, K., Murakoshi, H., Jacobson, K., and Kusumi, A. (2002). Phospholipids undergo hop diffusion in compartmentalized cell membrane. J. Cell Biol. *157*, 1071–1081.

Ghosh, S., Saha, S., Goswami, D., Bilgrami, S., and Mayor, S. (2012). Dynamic imaging of homo-FRET in live cells by fluorescence anisotropy microscopy. Methods Enzymol. *505*, 291–327.

Gimona, M., Djinovic-Carugo, K., Kranewitter, W.J., and Winder, S.J. (2002). Functional plasticity of CH domains. FEBS Lett. *513*, 98–106.

Goswami, D., Gowrishankar, K., Bilgrami, S., Ghosh, S., Raghupathy, R., Chadda, R., Vishwakarma, R., Rao, M., and Mayor, S. (2008). Nanoclusters of GPI-anchored proteins are formed by cortical actin-driven activity. Cell *135*, 1085–1097.

Gowrishankar, K. (2009). Dynamics of shape and composition of an active composite membrane. PhD thesis, Jawaharlal Nehru University, Bangalore, India.

Haviv, L., Brill-Karniely, Y., Mahaffy, R., Backouche, F., Ben-Shaul, A., Pollard, T.D., and Bernheim-Groswasser, A. (2006). Reconstitution of the transition from lamellipodium to filopodium in a membrane-free system. Proc. Natl. Acad. Sci. USA *103*, 4906–4911.

Howard, J. (2001). Mechanics of motor proteins and the cytoskeleton (Sunderland, MA: Sinauer Associates).

Jaqaman, K., Loerke, D., Mettlen, M., Kuwata, H., Grinstein, S., Schmid, S.L., and Danuser, G. (2008). Robust single-particle tracking in live-cell time-lapse sequences. Nat. Methods *5*, 695–702.

Kaizuka, Y., Douglass, A.D., Varma, R., Dustin, M.L., and Vale, R.D. (2007). Mechanisms for segregating T cell receptor and adhesion molecules during immunological synapse formation in Jurkat T cells. Proc. Natl. Acad. Sci. USA *104*, 20296–20301.

Kholodenko, B.N., Hancock, J.F., and Kolch, W. (2010). Signalling ballet in space and time. Nat. Rev. Mol. Cell Biol. *11*, 414–426.

Köhler, S., Schaller, V., and Bausch, A.R. (2011). Structure formation in active networks. Nat. Mater. *10*, 462–468.

Lingwood, D., and Simons, K. (2010). Lipid rafts as a membrane-organizing principle. Science *327*, 46–50.

Mayor, S., and Rao, M. (2004). Rafts: scale-dependent, active lipid organization at the cell surface. Traffic *5*, 231–240.

Morone, N., Fujiwara, T., Murase, K., Kasai, R.S., Ike, H., Yuasa, S., Usukura, J., and Kusumi, A. (2006). Three-dimensional reconstruction of the membrane skeleton at the plasma membrane interface by electron tomography. J. Cell Biol. *174*, 851–862.

Okreglak, V., and Drubin, D.G. (2010). Loss of Aip1 reveals a role in maintaining the actin monomer pool and an in vivo oligomer assembly pathway. J. Cell Biol. *188*, 769–777.

Plowman, S.J., Muncke, C., Parton, R.G., and Hancock, J.F. (2005). H-ras, K-ras, and inner plasma membrane raft proteins operate in nanoclusters with differential dependence on the actin cytoskeleton. Proc. Natl. Acad. Sci. USA *102*, 15500–15505.

Press, W.H., Teukolsky, S.A., Vetterling, W.T., and Flannery, B.P. (2007). Numerical Recipes: The Art of Scientific Computing (New York: Cambridge University Press).

Ramaswamy, S. (2010). The Mechanics and Statistics of Active Matter. Annu. Rev. Cond. Matt. Phys. *1*, 323–345.

Saarikangas, J., Zhao, H., and Lappalainen, P. (2010). Regulation of the actin cytoskeleton-plasma membrane interplay by phosphoinositides. Physiol. Rev. *90*, 259–289.

Saleh, H.S., Merkel, U., Geissler, K.J., Sperka, T., Sechi, A., Breithaupt, C., and Morrison, H. (2009). Properties of an ezrin mutant defective in F-actin binding. J. Mol. Biol. *385*, 1015–1031.

Sharma, P., Varma, R., Sarasij, R.C., Ira, Gousset, K., Krishnamoorthy, G., Rao, M., and Mayor, S. (2004). Nanoscale organization of multiple GPI-anchored proteins in living cell membranes. Cell *116*, 577–589.

Sheetz, M.P., Sable, J.E., and Döbereiner, H.G. (2006). Continuous membrane-cytoskeleton adhesion requires continuous accommodation to lipid and cytoskeleton dynamics. Annu. Rev. Biophys. Biomol. Struct. *35*, 417–434.

Simons, K., and Ikonen, E. (1997). Functional rafts in cell membranes. Nature *387*, 569–572.

Spudich, A., Wrenn, J.T., and Wessells, N.K. (1988). Unfertilized sea urchin eggs contain a discrete cortical shell of actin that is subdivided into two organizational states. Cell Motil. Cytoskeleton *9*, 85–96.

Suzuki, K.G., Fujiwara, T.K., Edidin, M., and Kusumi, A. (2007). Dynamic recruitment of phospholipase C gamma at transiently immobilized GPI-anchored receptor clusters induces IP3-Ca2+ signaling: single-molecule tracking study 2. J. Cell Biol. *177*, 731–742.

Svitkina, T.M., and Borisy, G.G. (1999). Arp2/3 complex and actin depolymerizing factor/cofilin in dendritic organization and treadmilling of actin filament array in lamellipodia. J. Cell Biol. *145*, 1009–1026.

Toner, J., and Tu, Y.H. (1998). Flocks, herds, and schools: A quantitative theory of flocking. Phys. Rev. E Stat. Phys. Plasmas Fluids Relat. Interdiscip. Topics *58*, 4828–4858.

van Zanten, T.S., Cambi, A., Koopman, M., Joosten, B., Figdor, C.G., and Garcia-Parajo, M.F. (2009). Hotspots of GPI-anchored proteins and integrin

nanoclusters function as nucleation sites for cell adhesion. Proc. Natl. Acad. Sci. USA *106*, 18557–18562.

Varma, R., and Mayor, S. (1998). GPI-anchored proteins are organized in submicron domains at the cell surface. Nature *394*, 798–801.

Varma, R., Campi, G., Yokosuka, T., Saito, T., and Dustin, M.L. (2006). T cell receptor-proximal signals are sustained in peripheral microclusters and terminated in the central supramolecular activation cluster. Immunity *25*, 117–127.

Verkhovsky, A.B., Svitkina, T.M., and Borisy, G.G. (1997). Polarity sorting of actin filaments in cytochalasin-treated fibroblasts. J. Cell Sci. *110*, 1693–1704.

Wan, C., Kiessling, V., and Tamm, L.K. (2008). Coupling of cholesterol-rich lipid phases in asymmetric bilayers. Biochemistry *47*, 2190–2198.

Yu, C.H., Law, J.B., Suryana, M., Low, H.Y., and Sheetz, M.P. (2011). Early integrin binding to Arg-Gly-Asp peptide activates actin polymerization and contractile movement that stimulates outward translocation. Proc. Natl. Acad. Sci. USA *108*, 20585–20590.